Probing the Nucleation Mechanism for the Binary *n*-Nonane/1-Alcohol Series with Atomistic Simulations

Ricky B. Nellas, Matthew E. McKenzie, and Bin Chen*

Department of Chemistry, Louisiana State University, Baton Rouge, Louisiana 70803-1804

Received: April 18, 2006; In Final Form: July 13, 2006

The AVUS−HR approach, which combines histogram reweighting with aggregation-volume-bias Monte Carlo nucleation simulations using self-adaptive umbrella sampling, was extended to multicomponent nucleation systems. It was applied to investigate the homogeneous vapor−liquid nucleation for the binary *n*-nonane/1-alcohol series, including the *n*-nonane/methanol, *n*-nonane/ethanol, *n*-nonane/1-propanol, *n*-nonane/1-butanol, *n*-nonane/1-hexanol, and *n*-nonane/1-decanol systems. The simple transferable potentials for phase equilibria-united atom force field was used in this investigation. It was found that the nucleation free energy (NFE) contour plots obtained for these binary *n*-nonane/1-alcohol nucleation systems exhibit rather interesting mechanistic features, some of which are distinct from other binary systems previously studied (such as water/ethanol and water/*n*-nonane). In addition, the NFE profiles show a subtle evolution with the increase in alcohol chain length, from a somewhat two-pathway type of shape as observed for the *n*-nonane/methanol system to a more normal single-pathway one for systems involving longer alcohols (1-hexanol and 1-decanol). In contrast, the NFE maps obtained for the other three binary systems involving those medium-length alcohols display the most striking feature with the saddle point stretched almost all the way from the *n*-nonane-enriched to the alcohol-enriched domain, implying that multiple pathways coexist on the nucleation map. These free energy profiles were shown to be consistent with the non-ideal nucleation behavior observed experimentally for this binary series, namely, a rather reluctant conucleation of the alcohols with *n*-nonane. In particular, this non-ideal behavior becomes more severe with a decrease in the alcohol chain length. Also, analysis of the compositions of the critical nuclei indicates a reluctant mixing behavior between these two species, i.e., depletion of the alcohol at low alcohol activity or depletion of *n*-nonane at low *n*-nonane activity, in agreement with the experimental interpretations. Furthermore, a microscopic inhomogeneity is present inside these critical nuclei, that is, alcohols aggregate via hydrogen bonds forming alcohol-enriched domains.

1. Introduction

Understanding the nucleation phenomenon wherein embryos of a new phase emerge from a metastable supersaturated mother phase is key to describe many processes of atmospheric, environmental, and technological importance. Multicomponent nucleation is of particular interest in this regard, as multiple condensable species are often involved in these processes. Hence, a great deal of experimental and theoretical research has been focused on this topic. These efforts have led to the recent emergence of sophisticated experimental techniques that allow measurement of nucleation rates with unprecedented accuracy not only for unary systems but also for binary and multicomponent systems.[1−16] In parallel, novel theoretical[16−24] (e.g., density functional theory) and simulation[25−34] methods have been put forward for a more accurate description of such phenomena. In particular, recent breakthrough in simulation methods is transforming molecular simulation as a complementary tool to study these nucleation events using realistic, atom-based models.[32−34]

In this work, the AVUS−HR approach,[34] which was developed previously for single-component nucleation systems by combining histogram reweighting with the aggregation-volume-bias Monte Carlo and self-adaptive umbrella sampling techniques, was extended to multicomponent nucleation systems.

It was applied to investigate the homogeneous vapor−liquid nucleation for the binary *n*-nonane/1-alcohol series, including *n*-nonane/methanol, *n*-nonane/ethanol, *n*-nonane/1-propanol, *n*-nonane/1-butanol, *n*-nonane/1-hexanol, and *n*-nonane/1-decanol. This study was partly initiated by our previous simulation on *n*-nonane/ethanol, for which a striking discovery of a multipathway mechanism was interpreted from the calculated nucleation free energy (NFE) profile.[35] We chose to investigate the *n*-nonane/1-alcohol series in a more detailed manner to specifically examine how the nucleation behavior evolves when the system approaches the macroscopic miscibility gap. It is well-known that the miscibility between *n*-nonane and 1-alcohol slowly changes with the chain length of the alcohol. In fact, *n*-nonane and methanol already exhibit a miscibility gap at the nucleation condition considered here. Also, this study was inspired by the experimental results obtained by Viisanen et al.[5] In particular, they discovered an unusual type of non-ideal nucleation behavior for this binary series compared to other non-ideal binary systems (such as water/ethanol) that they examined before. Normally, for macroscopically miscible fluids, the nucleation rate is expected to increase with the addition of the second component. However, for the *n*-nonane/alcohol systems, the nucleation rate was found to remain relatively undisturbed with the addition of the second component, even when the normalized activity of the second component is more than half of the first component in some cases. This behavior

* Corresponding author. E-mail: binchen@lsu.edu.

seems to resemble the water/*n*-nonane system, an immiscible mixture in both macroscopic and microscopic lengths,[33] which questions whether *n*-nonane and alcohol conucleate. Furthermore, such tendency to demix is in sharp contrast to the macroscopic miscibility known for most of these mixtures. The reluctant nucleation is even present, although less severe, in the *n*-nonane/1-hexanol system (1-hexanol is the longest alcohol molecule studied by them). In addition, they raised an open question on the orientation of OH groups of the alcohol molecules. Here we report on a simulation study to directly address the questions posed by the experimentalists as well as to provide a detailed view of the nucleation mechanism for these systems.

In the next section, the technical details and some further improvement of the AVUS−HR nucleation simulation approach are presented. In section 3, the molecular models (force fields) and other simulation details of this study are briefly described. The simulation results are presented and discussed in section 4, and section 5 provides concluding remarks.

2. Simulation Methods

A. Extension of the AVUS−HR Approach to Multicomponent Nucleation Systems. By combining aggregation-volume-bias Monte Carlo (AVBMC),[36,37] umbrella sampling (US),[38] and histogram reweighting (HR)[39,40], the resulting AVUS−HR approach delivers superior efficiency for the simulation study of rare nucleation events.[34] As mentioned previously,[34,35] the key to this success is that this method can overcome the several types of sampling difficulties encountered in the nucleation systems, including the large free-energy barriers (or low probabilities for the occurrence of clusters near the critical nucleus size) and the inherent microheterogeneity of the phase space (i.e., coexistence of clusters and monomers). The incorporation of the configuration-bias Monte Carlo (CBMC) scheme[41−43] further improves the acceptance rates for particle exchanges and, most importantly, allows the extension of this method to molecules with articulated structures. In addition, considering that large energy fluctuations are expected for the small clusters sampled in the nucleation simulations, it is natural to integrate HR[39,40] with this nucleation technique. Through HR, information can be extracted not only for the thermodynamic state under investigation but also for other neighboring thermodynamic states *without* additional simulations. If nucleation data are needed for low temperatures where phase-space sampling usually becomes difficult, HR can be combined with high-temperature simulations (where NFE data can be converged faster) to expedite the construction of the initial biasing potentials used for simulations at those more challenging conditions.

Previously, we implemented the AVUS−HR technique in the study of single-component nucleation events.[34] The generalization of this to multicomponent nucleation is straightforward except for some modifications on the computation of the density-of-states (DOS) histograms. For example, in a binary system for a cluster with a given composition (n_1, n_2), where n_1 and n_2 denote the number of molecules for type 1 and 2, respectively, the DOS histograms $\Omega_{(n_1,n_2)}(E)$ can be constructed from the simulations as follows:

$$\Omega_{(n_1,n_2)}(E) = P_{(n_1,n_2)}(E) \times e^{(-n_1\mu_1 - n_2\mu_2 + E)/k_BT} \qquad (1)$$

where $P_{(n_1,n_2)}(E)$ is the absolute probability density (expressed in terms of droplets per cubic angstrom) to observe this cluster with an intermolecular energy value of E, μ_1 and μ_2 are the

gas-phase (monomer) chemical potentials for type 1 and 2, respectively, k_B is Boltzmann's constant, and T is the absolute temperature. With these DOS histograms $\Omega_{(n_1,n_2)}(E)$, we can extract the absolute probability density at any other given gas-phase chemical potentials (μ_1^* and μ_2^*) and temperature ($T^* = T + \Delta T$) using the following equation:

$$P_{(n_1,n_2)}^* = \int \Omega_{(n_1,n_2)}(E) \times e^{[(n_1\mu_1^* + n_2\mu_2^* - E)/k_BT^*]}dE \qquad (2)$$

Correspondingly, the NFE formation of this cluster can be calculated from

$$\Delta G_{(n_1,n_2)}^* = -k_BT^* \ln[P_{(n_1,n_2)}^*(E)] \qquad (3)$$

Such extrapolation is valid provided that there are significant overlaps of the states sampled at these two different temperatures. Typically for the cluster-size range of our interest, the extrapolated results were found acceptable if T^* ranges from $T - 30$ K to $T + 30$ K.

B. Further Improvement on the AVUS−HR Technique. For hydrogen-bonded systems, local orientational heterogeneity is another important type of microheterogeneity that cannot be fully dealt with by the current AVBMC implementation, where the associating volume is defined as a spherical region centered around a given site of the molecule selected randomly from the cluster phase. Correspondingly, the acceptance rate of the AVBMC swaps deteriorates for these specific systems. This problem becomes even more severe for long-chain alcohols and at low temperatures. Intuitively, to overcome this problem, one might include another layer of definition to the aggregation volume, namely, an angular criterion, in a similar vein to other biased Monte Carlo methods.[44,45] For example, instead of using an isotropic sphere, this volume can be defined by a cone-shaped region (as preferred by these molecules), and the angular cutoff can be estimated a priori from the orientational distribution functions. The use of a cone-shaped volume certainly leads to a better balance of the different energetic and entropic factors exhibited by the cluster and monomer. However, the chance of successful insertion remains low due to the fact that most of these cone-shaped regions are occupied by other existing molecules. Thus, a successful implementation of this idea requires a sophisticated elaboration of the available bonding regions, which is not only technically complicated but also system specific.

Here we turn our focus to the reverse part of this problem: particle deletion. While locating the favorable associating regions is the bottleneck for particle insertion, for the deletion move, the strong association energies that most particles possess are responsible for the low acceptance rate observed as the acceptance probability decays exponentially with the decrease in the association energy of the particle to be deleted. To enhance the chance of successful deletion, it would be desirable to preferentially pick those particles with higher association energies rather than selecting them randomly. One way to implement this is to pick particles by the probability that is in direct proportion to $\exp(E_i/k_BT)$, where E_i is the association energy of a given particle i. For convenience, we use the commonly known Gibbs ensemble Monte Carlo (GEMC)[46−48] for illustration (as there is an intrinsic connection between AVBMC and GEMC). Suppose box a corresponds to our target high-density bulk phase; conventionally, the deletion move would be performed on a randomly selected particle (say, particle j) with a selection probability of $1/N$ where N is the number of particles within this box. On the contrary, in the

devised scheme, particle *j* is selected according to the following probability:

$$P_j = \frac{\exp(E_j/k_B T)}{W} \tag{4}$$

where

$$W = \sum_{i=1}^{N} \exp(E_i/k_B T) \tag{5}$$

To ensure the detail balance condition, this biased selection factor needs to enter the acceptance rule. For particle deletion, a factor of W/P_j will replace the factor of N present in the original acceptance formula. Similarly, for the reverse move (e.g., inserting particle *k*) into box *a* with the same configuration, a factor of $P_k/(W + P_k)$ will replace the factor of $1/(N + 1)$. The implementation of this energy-biased (EB) particle selection strategy into the AVUS−HR scheme is straightforward. While this addition leads to great improvement in the acceptance rate for particle swaps (as shown later in section 4A), the revised version retains the simplicity and generality of the original AVBMC algorithm.

3. Simulation Details

A. Molecular Models. In all calculations, the transferable potentials for phase equilibria-united atom (TraPPE-UA) force field[49,50] was used for its simplicity. The TraPPE-UA force field yields both single- and multicomponent phase diagrams that are in good agreement with the experimental data.[43,49−51] Previous simulations on single-component nucleation of *n*-heptane using the TraPPE-UA force field have shown that this force field overestimates the nucleation rate by a few orders of magnitude (or less than 10 $k_B T$ in terms of NFE barrier heights).[32] However, nucleation properties are extremely sensitive to molecular interactions.[34] Although quantitative comparison to experiments is still deemed as a challenge to molecular simulation for properties such as nucleation rates, previous simulations using this force field have shown that it was able to reproduce the non-ideal nucleation behavior observed for such non-ideal binary systems.[33,35]

B. Test Simulations Using the EB Particle Selection Scheme. The EB scheme was tested for a plethora of different scenarios, including the vapor−liquid phase equilibrium calculations employing the GEMC method and the NFE calculations using the AVUS−HR technique. These calculations were carried out for both polar and nonpolar systems at relatively low temperatures (248 K for *n*-heptane and 300 K for water and ethanol), where very poor acceptance rates were noticed for swap moves using the conventional particle selection scheme. For these systems, the phase space was sampled through the following Monte Carlo moves: translations, rotations, conformational changes using CBMC (except water for which a rigid TIP4P model was employed), and particle swaps. Volume moves were also used in the GEMC simulation, for which the frequency was adjusted to yield approximately one accepted move per 10 Monte Carlo cycles. For the GEMC simulations on water and ethanol, the frequency of the swap moves was also adjusted to yield approximately one accepted move per 10 Monte Carlo cycles, while, for the rest of the calculations, particle swaps contribute 40−50% to the total Monte Carlo moves. The remainder of moves were equally divided among translations and rotations (as well as conformational changes for ethanol and *n*-heptane). The production run consists of $O(10^9)$ Monte

Carlo moves. All pair interactions were included in the calculation of the total energy in the NFE studies. For the GEMC simulations, spherical potential truncation for both Lennard-Jones (LJ) and Coulombic interactions and analytical tail corrections[52] for the LJ part of the potential were employed.

C. NFE Calculations. For computational efficiency, all simulations were carried out using the grand-canonical version of the nucleation algorithm,[31] where the interactions between the cluster and the gas phase are neglected. As demonstrated previously, this approximation is acceptable in the low-temperature and low-density cases where these interactions are negligible.[32] Since *n*-alkane and 1-alcohol are chain molecules, following ref 24, an energy-based Stillinger-type cluster criterion was employed, in which a cluster is defined as a group of molecules in which every molecule has at least one neighbor in the group with an interaction energy less than U_{cl}. On the basis of prior experience with these systems, a U_{cl} of −260 K (close in magnitude to the simulation temperature) was chosen for all pairs of like molecules, whereas a U_{cl} of −120 K was used for all pairs of unlike molecules. It has been shown previously that the NFE results are relatively insensitive to the choice of the cutoff criterion.[32−34]

For the *n*-nonane/ethanol, *n*-nonane/1-hexanol, and *n*-nonane/1-decanol systems, simulations were carried out without the use of the EB scheme. Instead, the HR technique combined with high-temperature simulations was applied to facilitate the convergence of the NFE data. Simulations were initially carried out at $T = 300$ K where relatively short simulation runs ($O(10^8)$ Monte Carlo moves) were used in the iterations for the convergence of the NFEs or the biasing potential. Once the NFEs (or the biasing potential) have been converged for clusters of all sizes of interest, a simulation run consisting of 10^9 Monte Carlo moves is used to obtain the DOS histograms (using eq 1 with a bin width of $20 k_B$ K). From these histograms, the NFE results were extrapolated at a temperature lower by about 30 K using eqs 2 and 3. These extrapolated NFE results served as an initial guess for constructing the biasing potentials for simulations at this lower temperature. They were further smoothed through one to two quick iterations, followed by a longer production run where the DOS histograms were calculated again for another extrapolation of the NFE results at an even lower temperature. This iterative extrapolation procedure was continued (usually one more time) until the NFE results were obtained at the temperature where the experiments were carried out, 230 K. It should be noted that the simulation length needs to increase gradually with the decrease in the temperature to compensate for the loss of the acceptance rate on the AVBMC swaps. This was achieved by using multiple independent simulations (as many as 32 for the lowest temperature 230 K) that ran in parallel on different processors—a natural parallelization scheme in Monte Carlo. Since each of them started from a different configuration, this strategy also helps to ensure the sampling of clusters of all sizes/compositions of interest.

For the other three binary systems, simulations were directly carried out at 230 K with the use of the EB scheme. The initial biasing potential was constructed based on the NFE data already obtained for the former three systems. For example, for the *n*-nonane/1-butanol system, the following procedure was used. First, the NFE results were interpreted at the same combination of *n*-nonane and alcohol gas-phase densities for both *n*-nonane/ethanol and *n*-nonane/1-hexanol systems. Then these NFE values were averaged between these two systems for each cluster containing the same number of *n*-nonane and alcohol molecules.

18622 *J. Phys. Chem. B, Vol. 110, No. 37, 2006*

Nellas et al.

The averaged NFE data were used as an initial guess of the biasing potential for the *n*-nonane/1-butanol simulation.

All pair interactions (including both LJ and Coulombic) were included in the computation of the total energy of the cluster. The type of Monte Carlo move was selected at random according to the following probabilities: particle insertion (20%), particle deletion (20%), conformational changes using CBMC (10%), translation (25%), and rotation (25%). These moves were equally shared between the two molecular types present in the binary mixtures except for the AVBMC-enhanced particle insertion/deletion moves. Because a much higher acceptance rate (by about an order of magnitude) was observed for the AVBMC moves on *n*-nonane relative to that on alcohol molecules, 90% of the AVBMC moves were performed on alcohol, and the rest (10%) were performed on *n*-nonane to enable a comparable number of swap moves accepted for both types of molecules.

D. Determination of Onset Activities. Experimentally, the onset activities correspond to those that yield a fixed nucleation rate.[5] Here, a constant nucleation barrier height was used to construct the onset activity plots, similar to previous simulation studies.[33,35] Although the conversion between the nucleation barrier and the nucleation rate requires the knowledge of an additional preexponential factor, this kinetic factor depends only weakly on the vapor-phase activities. Following a previous analysis performed on the *n*-nonane/ethanol system, a combined nucleation barrier was employed, which allows one to account for the contributions from more than one nucleation pathway present on the NFE map. In the calculations of this combined barrier, the NFE profiles (two-dimensional diagrams originally plotted as a function of the numbers of molecules for the two components) were projected onto a single coordinate, the combined size of the cluster. Thus, for a cluster with a total size of *n*, its free energy formation is calculated as follows:

$$\exp[-\Delta G^{\text{tot}}(n)/k_{\text{B}}T] = \sum_{n_1=0}^{n} \exp[-\Delta G(n_1, n - n_1)/k_{\text{B}}T] \quad (6)$$

With this one-dimensional plot, the determination of the barrier height and critical cluster size is straightforward (similar to single-component nucleation). A value of around 50.64 $k_{\text{B}}T$ for the barrier height, which corresponds to a concentration of 100 droplets/cm³ for the critical nuclei, was chosen to plot the onset activities for our simulation. For both *n*-nonane and ethanol, this critical cluster concentration is about to yield a nucleation rate of 10^7 droplets/cm³/s, based on the following classical expression[53] for the nucleation rate, *J*, for single-component systems in terms of the critical cluster concentration ρ_{n^*}:

$$J = \frac{\rho_{\text{vap}}^2}{\rho_{\text{liq}}S}\left(\frac{2\gamma}{\pi m}\right)^{1/2}\exp(-\beta\Delta G^*) = \frac{\rho_{\text{vap}}}{\rho_{\text{liq}}S}\left(\frac{2\gamma}{\pi m}\right)^{1/2}\rho_{n^*} = J_0\rho_{n^*} \quad (7)$$

where ρ_{vap} and ρ_{liq} are the densities of the supersaturated vapor and the liquid phase at coexistence, respectively, *S* is the supersaturation, γ is the surface tension, *m* is the molecular mass, and ΔG^* is the nucleation barrier height (relative to the monomer's free energy). The term $\rho_{\text{vap}}/(\rho_{\text{liq}}S)$ can be approximated by the ratio of the saturated vapor-phase density to the liquid-phase density. Using the experimental coexistence densities, J_0 is estimated to be around $O(10^5)$ s⁻¹ for both *n*-nonane and ethanol at 230 K.

4. Simulation Results and Discussions

A. Effect of the EB Particle Selection Scheme on the Acceptance Rate. The EB selection scheme is designed to allow
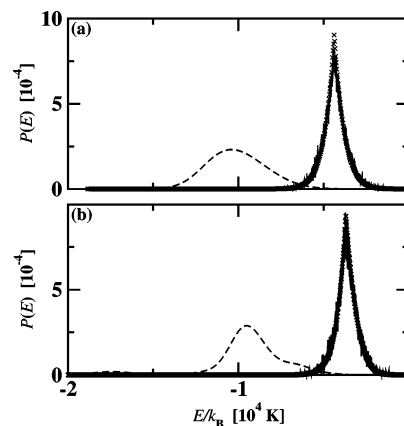

Figure 1. Molecular energy distributions for the water (a) and ethanol (b) systems obtained from the GEMC simulations at 300 K by averaging over all the molecules in the bulk phase (dashed lines, denoted as $P_1(E)$) or over only those molecules that have been successfully deleted from the bulk during the swap moves (solid lines, denoted as $P_2(E)$). $P_2(E)$ can be fitted very well by the curve (shown as crosses, $P_3(E)$) obtained by multiplying $P_1(E)$ with the projected acceptance rate of min{1, exp[($E - E_t$)/$k_{\text{B}}T$]} and normalized afterward.

TABLE 1: Acceptance Rates (Acc) in % Obtained for Various Systems from Both GEMC and AVBMC Nucleation Simulations with and without the EB Particle Selection Scheme

method	GEMC			AVBMC		
molecular type	*n*-heptane	water	ethanol	*n*-heptane	water	ethanol
system size	300	500	500	1−80	1−80	1−80
Acc (with EB)	0.007	1.2	2.6	15.5	6.3	4.4
Acc (without EB)	0.003	0.1	0.3	7.4	1.1	0.8

preferential selection of those particles with higher association energies for deletion to enhance the acceptance rate. This scheme is particularly effective for hydrogen-bonded systems (such as water and alcohol) since, for these systems, most molecules in the interior of the bulk appear to have an association energy far below the deletable threshold. As shown in Figure 1, the molecular energy distributions for the deletable particles ($P_2(E)$) are peaked at significantly higher energy values (around −4380 K for water and −3700 K for ethanol) compared to those distributions averaged over all molecules ($P_1(E)$) in the bulk phase. These most probable energy values found for the deletable particles can be viewed as the energetic threshold (E_t) for particle deletion from the bulk; that is, the acceptance rate approaches unity exponentially as the association energy of the particle increases to E_t. In fact, using a projected acceptance rate of min{1, exp[($E - E_t$)/$k_{\text{B}}T$]} multiplied by $P_1(E)$, the resulting curve $P_3(E)$, if normalized, yielded a nearly perfect fit to $P_2(E)$ (see Figure 1). On the other hand, before normalization, this combined curve $P_3(E)$ provided a quick estimate of the absolute acceptance rate contributed by molecules with a given energy *E*. Thus, the overall acceptance rate for the particle deletion move can be obtained by integrating this curve over all possible energy values. Indeed, following this procedure, a total acceptance rate of 0.19% and 0.37% was estimated for particle deletion from the liquid water and liquid ethanol, respectively, comparable to those values obtained directly from the simulations without the EB scheme (see Table 1), by simply dividing the number of successful deletions by the number of trials. This analysis also confirms our initial speculation, that is, the bottleneck for particle deletion from the liquid-phase originates from the strong association energies (far lower than the deletable threshold) that most particles possess.

The EB particle selection scheme allows one to partially overcome this problem. By preferentially selecting those

Nucleation Mechanism for *n*-Nonane/1-Alcohol

J. Phys. Chem. B, Vol. 110, No. 37, 2006 **18623**

TABLE 2: Densities (in units of g/mL) of the Coexisted Vapor and Liquid Phases Obtained from the GEMC Simulations with and without the EB Particle Selection Scheme[a]

system	$\rho_{vap} \times 10^5$		ρ_{liq}	
n-heptane at 248 K	2.8_1^b	2.9_1	0.726_1^b	0.726_2
water at 300 K	3.4_1^b	3.4_1	1.008_1^b	1.008_1
ethanol at 300 K	19.2_7^b	18.5_7	0.784_1^b	0.782_1

[a] The subscripts give the statistical accuracies of the last decimal. [b] Results with the EB scheme.
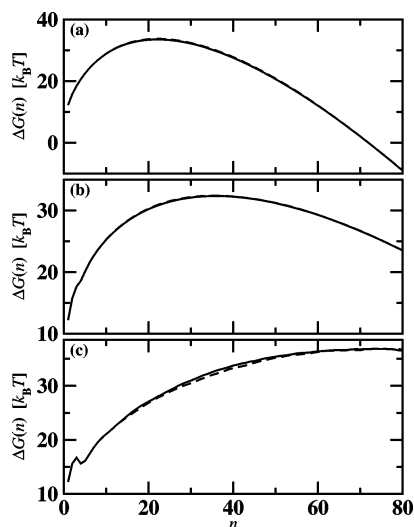
Figure 2. NFE results as a function of the cluster size obtained from the AVBMC simulations with (solid lines) and without (dashed lines) the EB particle selection scheme for (a) *n*-heptane at 248 K, (b) water at 300 K, and (c) ethanol at 300 K. All simulations were carried out at a gas-phase density $n_v = 5 \times 10^{-6}$ Å^{-3}.

particles with higher association energies (rather than picking them randomly in the conventional scheme), the chance of successful deletion is greatly enhanced. As shown in Table 1, nearly an order of magnitude improvement on the acceptance rates was observed for polar water and ethanol systems for simulations with the EB scheme compared to those without. Even for the nonpolar *n*-heptane system, appreciable gains (roughly a factor of 2) on the acceptance rates were obtained. This large improvement allows one to significantly reduce the total number of swap moves that need to be performed for these systems (in order to yield one accepted swap per 10 Monte Carlo cycles). As particle swaps are usually the most expensive type of Monte Carlo moves, the overall cost of the simulation with the EB scheme is actually lower than that without the EB scheme. While the acceptance rate of the swap moves is obviously improved with the use of the EB scheme, it is equally important to demonstrate that the equilibrium properties are sampled correctly. Compared in Table 2 and Figure 2 are the coexistence properties and NFE results calculated for the various systems between simulations with and without the EB selection scheme for the particle swaps. For all cases investigated, the results are in good agreement with each other within the statistical uncertainties.

B. NFE Contour Maps. Plotted in Figure 3 are the contours of the two-dimensional NFEs as a function of the number of *n*-nonane and alcohol molecules calculated for the various *n*-nonane/alcohol systems at a composition condition when both species contribute roughly equally to the nucleation event. For comparison, the NFE contours obtained previously[35] for the *n*-nonane/water and water/ethanol systems were also plotted in Figure 3. It is clear from this figure that the binary *n*-nonane/

1-alcohol nucleation systems exhibit rather unique mechanistic features that are distinct from the *n*-nonane/water and water/ethanol systems. Most noticeable is the widely open saddle point region that appears to stretch from the *n*-nonane-enriched domain to the alcohol-enriched domain. This is an indication that, for the *n*-nonane/1-alcohol systems, nucleation could proceed through multiple channels compared to the one or two noticed for the other binary systems. This feature is particularly prominent for those systems involving medium-length alcohols, such as ethanol, 1-propanol, and 1-butanol. In addition, by monitoring how this feature dissipates towards the two ends (either to the shortest alcohol (methanol) or to longer alcohols, such as 1-hexanol and 1-decanol), it is tempting to conclude that the appearance of this elongated saddle point region arises from a nearly perfect balance between the tendency to mix and the tendency to demix among the *n*-nonane and the alcohol molecules. For example, the rising of an island at the center of the saddle point region, as noted for the *n*-nonane/methanol system, is clearly a sign of demixing on a microscopic length between these two species, which is consistent with the macroscopic miscibility gap known for this mixture. This island apparently separates the saddle point region into two parts, which leads to a two-pathway type of nucleation map, resembling, to some extent, the one found for the *n*-nonane/water mixture. At the other end, the NFE maps for both *n*-nonane/1-hexanol and *n*-nonane/1-decanol systems display a more normal type of shape with the central part sunk (instead of rising, as compared to *n*-nonane/methanol) to become a "true" saddle point, although it is still elongated but to a lesser degree. This points to an enhanced mixing behavior between *n*-nonane and longer alcohol molecules (consistent with their better macroscopic miscibility), namely, the formation of a mixed critical nucleus is now more preferable than forming two types of phase-separated critical nuclei, similar to water/ethanol. On the other hand, for binary mixtures involving medium-length alcohols from ethanol to 1-butanol, the appearance of a highly elongated saddle point region is a result of a roughly equal probability of forming critical nuclei of all compositions (balanced by their tendencies to mix and demix). Another distinct feature for the *n*-nonane/alcohol systems is the appearance of the ellipsoidal island, mainly due to the formation of stable hydrogen-bonded alcohol complexes (i.e., cyclic pentamers).

The NFE maps shown in Figure 3 detail a rather subtle evolution of the miscibility between *n*-nonane and 1-alcohol with the increase in the alcohol chain length. This small-length scale information seems to parallel well with the available macroscopic miscibility data between these two species. Experimentally, methanol and *n*-nonane were shown to have a miscibility gap already at room temperature. Ethanol is fully miscible with *n*-nonane at room temperature but will approach a miscibility gap at lower temperatures.[5] With further increase of the alcohol chain length, an increasingly better miscibility with *n*-nonane is expected on a macroscopic length scale. Similarly, this trend was also observed for clusters on a much smaller length scale. Furthermore, this systematic study on the homogeneous nucleation of the homologous *n*-nonane/1-alcohol series reveals an interesting finding on how nucleation behaves when the system approaches the macroscopic miscibility gap. Namely, the nucleation event switches from a single-pathway mechanism (as observed for *n*-nonane/1-hexanol) to a two-pathway one (for *n*-nonane/methanol), while between it adopts a multi-pathway mechanism (for binary mixtures involving medium-length alcohols). Such a mechanistic switch was, to some extent, already captured by previous theoretical stud-
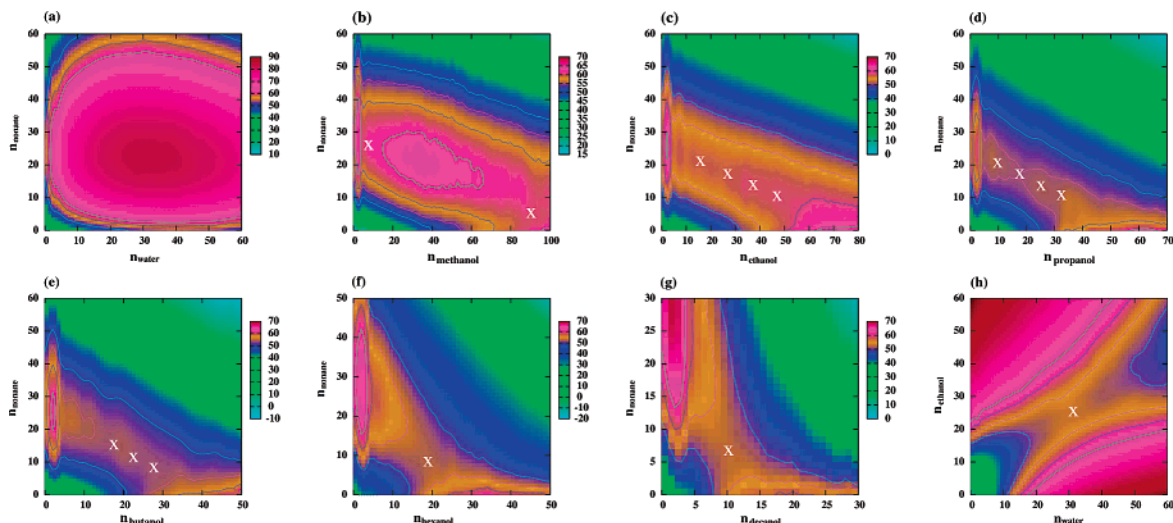
Figure 3. Contour of the two-dimensional NFEs (in units of k_BT) as a function of the number of molecules for the two components involved in each binary mixture calculated from the simulation at (a) $n_v^{nonane} = 1.71 \times 10^{-7}$ Å^{-3} and $n_v^{water} = 4.36 \times 10^{-8}$ Å^{-3}; (b) $n_v^{nonane} = 1.34 \times 10^{-7}$ Å^{-3} and $n_v^{methanol} = 8.11 \times 10^{-8}$ Å^{-3}; (c) $n_v^{nonane} = 1.45 \times 10^{-7}$ Å^{-3} and $n_v^{ethanol} = 3.83 \times 10^{-8}$ Å^{-3}; (d) $n_v^{nonane} = 1.58 \times 10^{-7}$ Å^{-3} and $n_v^{1-propanol} = 1.41 \times 10^{-8}$ Å^{-3}; (e) $n_v^{nonane} = 1.45 \times 10^{-7}$ Å^{-3} and $n_v^{1-butanol} = 5.71 \times 10^{-9}$ Å^{-3}; (f) $n_v^{nonane} = 1.26 \times 10^{-7}$ Å^{-3} and $n_v^{1-hexanol} = 6.87 \times 10^{-10}$ Å^{-3}; (g) $n_v^{nonane} = 1.11 \times 10^{-7}$ Å^{-3} and $n_v^{1-decanol} = 2.34 \times 10^{-11}$ Å^{-3}; and (h) $n_v^{ethanol} = 1.61 \times 10^{-8}$ Å^{-3} and $n_v^{water} = 1.71 \times 10^{-8}$ Å^{-3}. Some of the representative saddle points were shown as crosses except for the binary *n*-nonane/water system in which nucleation was found to proceed along the two axes (either via pure *n*-nonane or via pure water). A line of crosses is identified for binary mixtures involving medium-length alcohols, implying that multiple pathways coexist on the nucleation map. For a clear view of the NFE profiles near the saddle points, the contour levels with NFE values of 50, 54, 58, and 62 k_BT are depicted explicitly as lines.

ies[22,23,26,54,55] employing relatively simple models, such as Lennard-Jonesium (LJ). For example, in the simulation study carried out by ten Wolde and Frenkel[26] on binary LJ mixtures, it was found that nucleation proceeds via a single type of critical nuclei for fully miscible systems. For mixtures with a miscibility gap, nucleation could still proceed via a mixed nucleus but become more likely to adopt a two-pathway mechanism for larger cluster sizes or when their demixing tendency is enhanced through the change of the mixing parameter. In addition, they found that a regime exists for partially miscible mixtures, where the critical nuclei seem to be miscible in all proportions.

Although this mechanistic switch has been qualitatively reproduced by the early studies, the relatively simple LJ models employed therein did not allow direct, quantitative comparison with the experiments, especially considering that neither chain molecules nor the orientationally dependent hydrogen-bond interactions (involved by alcohols) can be sufficiently described via the use of a spherical LJ bead.[32] A benefit of using realistic, atom-based models (that were previously parametrized to experimentally known thermodynamic properties, such as phase equilibrium data) is that such models allow for a side-by-side comparison to the experimental nucleation data for various systems. This comparison is important, as some of the NFE maps obtained have challenged the theory with respect to whether a simplistic view of the nucleation process holds for all systems. In particular, those maps that show the coexistence of multiple nucleation channels are directly at odds with a fundamental assumption employed by the theory, that is, nucleation proceeds on a well-defined path via the formation of a critical nucleus with a well-defined structure and composition, upon which the theoretical formalism of the nucleation rate can be derived.[5,17–20] Thus, it needs to be verified that these contour plots are actually consistent with the non-ideal nucleation behavior observed experimentally for these systems.

C. Plots of the Onset Activities. Plotted in Figure 4 are the various combinations of onset activities for the vapor−liquid nucleation of the different *n*-nonane/1-alcohol mixtures,
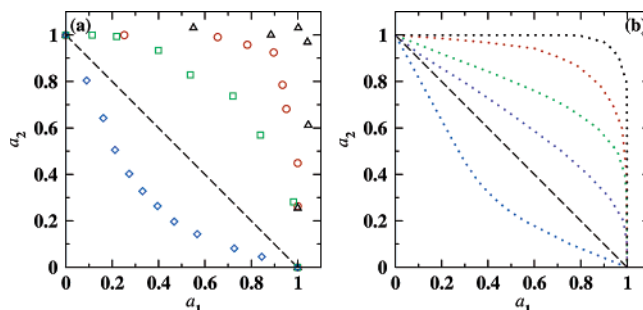

Figure 4. Plots of reduced onset activities. In the left panel are the experimental data[4−6] for binary *n*-nonane/ethanol, *n*-nonane/1-hexanol, *n*-nonane/water, and water/ethanol mixtures at a constant nucleation rate of 10^7 droplets/cm^3/s. Simulation counterparts (right panel) were drawn using dotted lines. The colors black, red, green, purple, and blue represent *n*-nonane/water, *n*-nonane/ethanol, *n*-nonane/1-hexanol, *n*-nonane/1-decanol, and water/ethanol, respectively. The ideal case would correspond to the dashed straight line. For binary systems involving *n*-nonane, a_1 refers to the *n*-nonane vapor phase activity and a_2 for the other component. For water/ethanol, a_1 and a_2 are the water and ethanol vapor phase activity, respectively.

including *n*-nonane/ethanol, *n*-nonane/1-hexanol, and *n*-nonane/1-decanol. These onset activities are normalized by the activities of neat *n*-nonane and neat 1-alcohol vapors and correspond either to a constant nucleation rate of 10^7 droplets/cm^3/s, as measured experimentally, or to a combined nucleation barrier height of around 50.64 k_BT, as calculated from the simulations (see section 3D). For comparison, the onset activity data obtained previously for the *n*-nonane/water and water/ethanol systems,[35] as well as the available experimental data[4−6] for these systems, are also plotted in Figure 4. It should be noted that the use of this combined barrier (defined in eq 6) naturally takes into account an important factor unique for these mixtures, namely, the size of the saddle-point region, since, in general, the larger this area, the greater the number of nucleation pathways, and the higher the nucleation rate. As is evident from this figure, both the experimental and simulation data show that
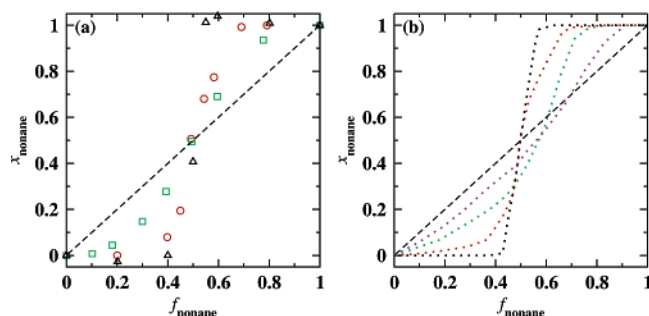
Figure 5. Average mole fraction of *n*-nonane in the critical nuclei as a function of the normalized activity fraction of *n*-nonane. Symbols and panels are the same as those in Figure 4.

Figure 6. Probability density (expressed as an absolute concentration) of the critical cluster nuclei as a function of $\delta = n_{\text{nonane}} - n_{\text{alcohol}}$ for the nucleation of *n*-nonane/methanol (cyan solid), *n*-nonane/ethanol (green dashed), *n*-nonane/1-decanol (purple dashed−dotted), and *n*-nonane/water (black dotted) at a normalized *n*-nonane activity fraction of 0.5 with a combined nucleation barrier height of 50.64 $k_{\text{B}}T$.

Figure 7. Probability density of the critical cluster (solid) and the precritical clusters containing 5 (dashed), 10 (dashed−dotted), and 15 (dotted) molecules as a function of $\delta = n_{\text{nonane}} - n_{1-\text{hexanol}}$ for nucleation of the binary *n*-nonane/1-hexanol system at a normalized *n*-nonane activity fraction of 0.5 with a combined nucleation barrier height of 50.64 $k_{\text{B}}T$.

nucleation of the *n*-nonane/1-alcohol occurs at much higher activities than expected for an ideal mixture, for which the reduced onset activities simply fall on a straight line and sum to unity. These higher onset activities signal a reluctant co-nucleation between *n*-nonane and 1-alcohols, which becomes more apparent if one compares these data to those for the *n*-nonane/water mixture, in which nucleation proceeds through a two-pathway mechanism (one via an *n*-nonane-enriched nucleus and the other via a water-enriched nucleus; see the NFE map shown in Figure 3). In addition, the simulation data semi-quantitatively reproduce the experimentally observed chain-length dependency of this non-ideal behavior; that is, the reduced onset activities lower gradually with the increase in the alcohol chain length and approach those for the ideal mixtures, although appreciable deviation from the ideal behavior is observed even for *n*-nonane/1-decanol, the longest alcohol investigated here. This evidence of increasing tendency to conucleate for longer alcohols with *n*-nonane is expected in view of their enhanced miscibility with each other, both macroscopically and micro-scopically (see discussions in section 4B). In sharp contrast, another fully miscible mixture, water/ethanol, shows an opposite behavior, with the onset activities curved to the other side, which was interpreted previously as a sign of mutual nucleation enhancement by both experiments[4] and the simulations.[33,35]

D. Molecular Content of Nuclei. The increasing non-ideality of the *n*-nonane/1-alcohol mixtures with the decreasing alcohol chain length is also evident from the composition diagrams for the critical nuclei shown in Figure 5. The composition for the critical nuclei was calculated through averaging the composition of all clusters with the critical cluster size weighted by their corresponding probability densities. Again, a very good agree-ment was found between the experiments and the simulations, with both showing that the composition of the critical nuclei evolves in a nonlinear way as a function of the normalized activity fraction, $f_{\text{nonane}} = (a_{\text{nonane}}/a_{\text{nonane}}^0)/(a_{\text{alcohol}}/a_{\text{alcohol}}^0 + a_{\text{nonane}}/a_{\text{nonane}}^0)$. The sigmoidal shape of these plots is a sign of a depletion of alcohol at low alcohol activity or a depletion of *n*-nonane at low *n*-nonane activity, providing additional evidence of the reluctant conucleation between these two species. The good agreement between the experiments and the simulations also seems to support the applicability of using the nucleation theorem[4,7,56,57] in the experimental interpretation of the content of the critical nuclei (i.e., determined from the slopes of the nucleation rate surface). However, it should be noted that this averaged molecular content, a single number, belies the miscibility information and the fact that a wide range of compositions could be present for the critical nuclei, as already indicated from the NFE contours shown in Figure 3. Therefore, it would be misleading to use this average content of the critical nuclei to locate the true saddle point in the nucleation pathway.
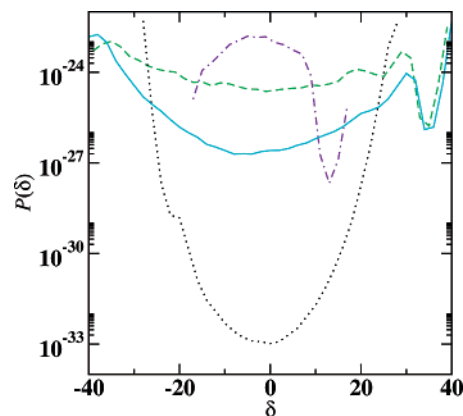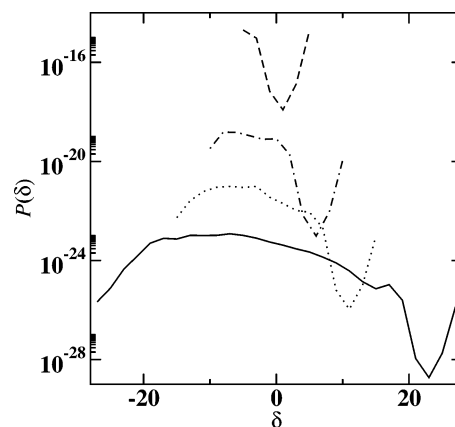
For example, in the case of an *n*-nonane/water mixture, an *n*-nonane mole fraction of close to 0.5 obtained at an f_{nonane} of 0.5 cannot be interpreted as the formation of a single mixed critical nucleus with equal molar amounts of the two components involved. Rather, this value appears to accidentally arise from the formation of two major critical nuclei, one *n*-nonane-enriched and the other water-enriched.

The same behavior may be expected for the *n*-nonane/1-alcohol systems. The situation becomes even more complicated because the critical nuclei were found to be miscible in all proportions for these cases. Fortunately, the simulations de-scribed here sample the entire spectrum of clusters (i.e., clusters of different sizes and all possible compositions), and thus allow a quantitative elaboration of these microscopic details. Plotted in Figure 6 are the density distributions for the critical cluster nuclei as a function of the composition at a normalized nonane activity fraction of 0.5. As expected, this plot switches from a concave shape for *n*-nonane/methanol to a convex shape for *n*-nonane/1-decanol, while between it is relatively more flat for *n*-nonane/ethanol (also for *n*-nonane/1-propanol and *n*-nonane/1-butanol, which were not shown here for clarity purposes). The concave shape with a dip centered around a δ ($= n_{\text{nonane}} - n_{\text{alcohol}}$) value of zero is a clear indication of demixing or a two-pathway nucleation mechanism that mimics the *n*-nonane/water
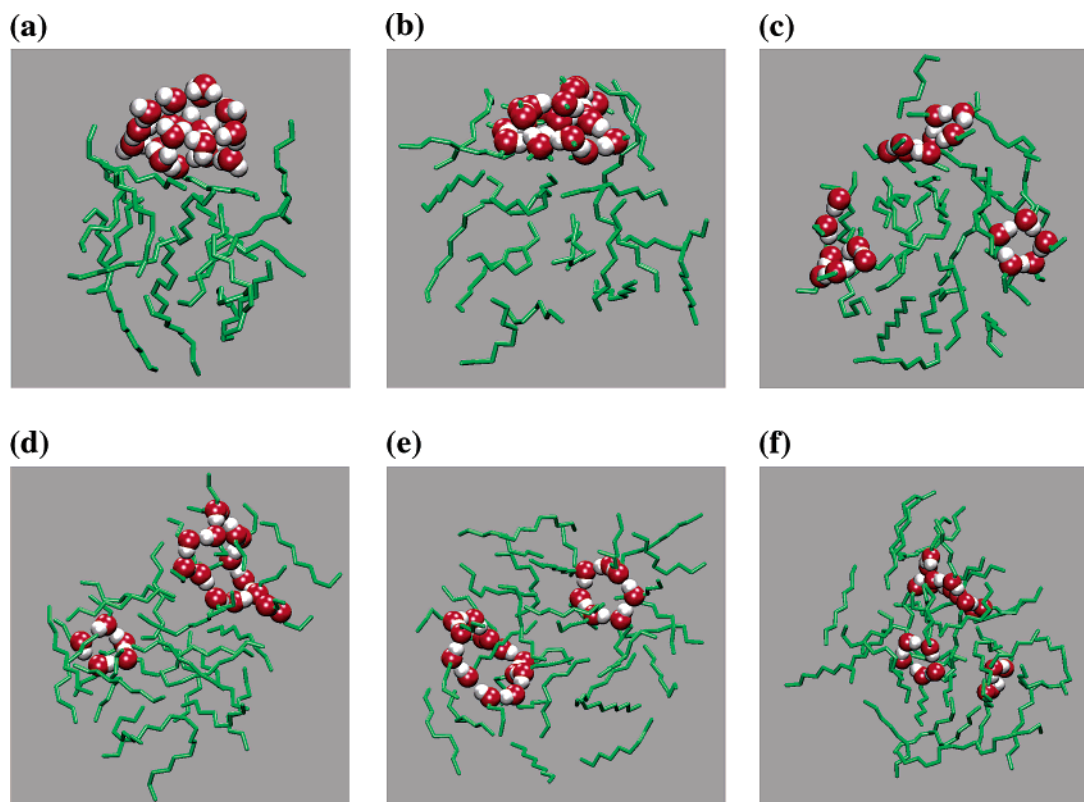
Figure 8. Representative snapshots of clusters (consisting of 20 *n*-nonane and 20 alcohol or water molecules) obtained at $T = 230$ K for (a) *n*-nonane/water, (b) *n*-nonane/methanol, (c) *n*-nonane/ethanol, (d) *n*-nonane/1-propanol, (e) *n*-nonane/1-butanol, and (f) *n*-nonane/1-hexanol. Oxygens and hydrogens are shown as a sphere in red and white, respectively. A stick representation is used for the alkyl tails.

system. Even for *n*-nonane/ethanol, the flat region seems to be dipped slightly in the middle, implying that a full miscibility remains unfavorable, despite the fact that the mole fraction of ethanol averaged over all the critical nuclei is close to 0.5 at this condition. On the other hand, the convex shape observed for longer alcohols with a maximum centered around the average nuclei composition signals an enhanced miscibility and a tendency to adopt a single-pathway nucleation mechanism. Such an evidence of enhanced miscibility even extends to small clusters with a few molecules (see Figure 7). However, irrespective of the alcohol chain length, clusters with a molecular content of around two alcohols are discouraged for all sizes. This is consistent with the ellipsoidal island present on the NFE contour maps shown in Figure 3. Both indicate that the initial mixing of alcohols with *n*-nonane needs to pass through this unfavorable phase (i.e., formation of alcohol dimers).

E. Microscopic Structures of Clusters. From visual inspection of cluster configurations (see Figure 8), it is immediately clear that, inside these clusters, there is another layer of microheterogeneity (apart from the major type of heterogeneity due to the presence of a wide spectrum of clusters), which arises from the aggregation of alcohol molecules through hydrogen-bonding interactions.[58,59] In fact, this aggregation leads to an internal "microphase separation" (see Figure 8). This feature is more prominent for systems involving shorter alcohols (such as methanol and ethanol) where the clusters typically exhibit a core/shell shape structure in which the hydrogen-bond aggregates attempt to wrap around the nonpolar core formed by the *n*-nonane molecules (see Figure 8c). Occasionally, these small aggregates further cluster together and form one large hydrogen-bond aggregate that leads to a fully phase-separated structure (see Figure 8b), resembling, to some extent, the double-layer structure observed for the *n*-nonane/water mixture (see

Figure 8a). On the contrary, as the hydrophobic chain length of the alcohol component increases, the hydrogen-bond aggregates tend to disperse inside the nonpolar domain formed by the *n*-nonane molecules (see Figure 8d−f). For longer alcohols, the alkyl tails can be preferentially solvated by *n*-nonane, which is the microscopic origin for the enhanced miscibility between these two species. Analysis of radial density profiles of mixed clusters containing a roughly equal number (20 ± 2) of *n*-nonane and 1-alcohol molecules also supported this picture (see Figure 9). For systems involving shorter alcohols (i.e., methanol or ethanol), there is a noticeable enrichment of the alcohol oxygen and hydrogen densities toward the surface, which is consistent with the core/shell structure pattern shown above. In contrast, for the *n*-nonane/1-hexanol system, the 1-hexanol oxygen and hydrogen density profiles shift substantially toward the center of the cluster, leading to an interior enrichment of the 1-hexanol carbon densities accompanied by a depletion of the *n*-nonane carbon densities.

Clearly, the formation of hydrogen-bond aggregates is the most important structural motif for clusters involving polar alcohol molecules. We further analyzed the distribution of the alcohol molecules over the aggregate size. In this analysis, a simple distance cutoff ($r_{OO} < 3.3$ Å)[60] was used to determine whether two alcohol molecules belong to the same hydrogen-bonded aggregate. The results were plotted in Figure 10. The overall distribution looks quite similar between the different alcohols studied here. In particular, a majority of these hydrogen-bonded aggregates consist of four to eight alcohol molecules with five as the most probable number. This is consistent with those representative snapshots and with the aforementioned presence of an ellipsoidal island on the NFE maps. In addition, the distribution is rather broad, which seems to suggest that a very diverse spectrum of hydrogen-bonded aggregates is present
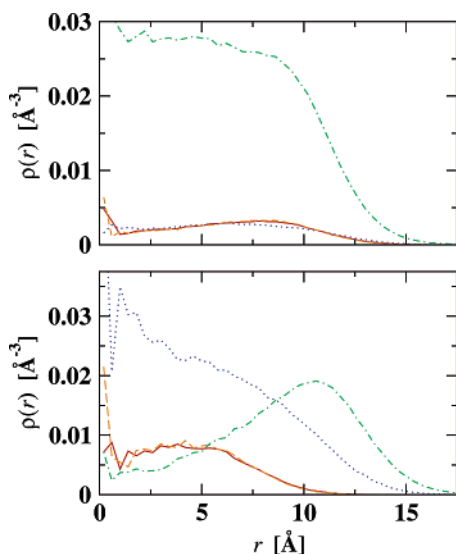
Nucleation Mechanism for *n*-Nonane/1-Alcohol

J. Phys. Chem. B, Vol. 110, No. 37, 2006 **18627**

Figure 9. Radial density profiles for the *n*-nonane/methanol (top) and *n*-nonane/1-hexanol (bottom) systems averaged over clusters containing a roughly equal number (20 ± 2) of *n*-nonane and 1-alcohol molecules. The red solid, orange dashed, blue dotted, and green dashed–dotted lines represent the number density profiles for the alcohol oxygen atoms, the alcohol hydrogen atoms, the alcohol carbon atoms, and the *n*-nonane carbon atoms, respectively.
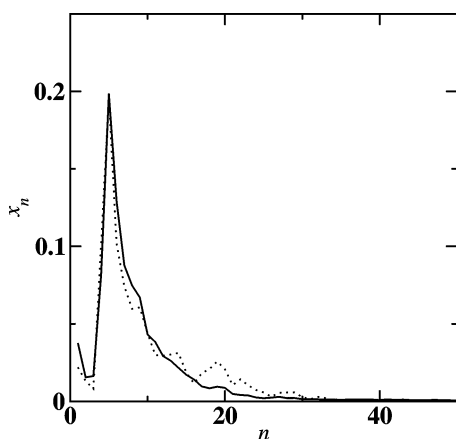

Figure 10. Distributions of 1-alcohol hydrogen-bonded aggregates with aggregation number *n* for *n*-nonane/methanol (solid) and *n*-nonane/1-hexanol (dotted) found in those clusters near the saddle-point region shown in Figure 3, i.e., with an NFE value between 58 and 62 k_BT for *n*-nonane/methanol or between 50 and 54 k_BT for *n*-nonane/1-hexanol.

inside these clusters. All these features already resemble those reported previously for the bulk alcohol phases.[50,60]

F. Further Discussions. Returning back to the open questions raised by the experimentalists,[5] from the detailed microscopic insights presented above, it is now clear that *n*-nonane and alcohol nucleate together under certain conditions by forming clusters containing both species. However, they mix with each other rather reluctantly. First, with a decrease in the alcohol chain length, we start to observe a trend of demixing with *n*-nonane, as evident from the concave shape exhibited by the composition diagram shown in Figure 6. This trend is consistent with the ultimate appearance of the macroscopic miscibility gap observed for the *n*-nonane/methanol mixture at this temperature. Second, even if they come together forming clusters, these two components tend to separate from each other microscopically because the polar OH groups of the alcohols will always point away from the nonpolar alkyl chains and bind to themselves through hydrogen bonds forming polar aggregates. For shorter

alcohols, further clustering of these aggregates would take place, leading to entirely phase-separated structures, like the double-layered one observed for *n*-nonane/methanol and *n*-nonane/ethanol.

5. Conclusions

In conclusion, the AVUS−HR approach was extended to multicomponent nucleation systems to allow calculation of the properties for binary vapor−liquid nucleation of *n*-nonane/methanol, *n*-nonane/ethanol, *n*-nonane/1-propanol, *n*-nonane/1-butanol, *n*-nonane/1-hexanol, and *n*-nonane/1-decanol mixtures at an ultralow temperature of 230 K. Using the TraPPE-UA force field, it was found that these simulations were able to reproduce the experimentally observed non-ideal nucleation behavior for this *n*-nonane/1-alcohol series, that is, a reluctant conucleation between them. In particular, with a decrease in the alcohol chain length, the onset activities were found to approach those for the *n*-nonane/water mixture (where independent nucleation was shown to take place), consistent with the experiments. Also, the calculated compositions on the critical nuclei agree with those interpreted from the slope of the experimental nucleation rate surface based on the nucleation theorem. Both indicate a reluctant mixing behavior between these two species, i.e., depletion of the alcohol at low alcohol activity or depletion of *n*-nonane at low *n*-nonane activity. However, caution is needed when using the average content of the critical nuclei to identify the true saddle point in the nucleation pathway, as a wide range of compositions were found to be present for the critical nuclei at certain conditions for the *n*-nonane/1-alcohol systems. Additional analysis on composition and structure further confirmed this reluctant mixing/conucleation behavior. More importantly, the calculated NFE maps reveal an interesting mechanistic switch for this *n*-nonane/1-alcohol series when approaching the miscibility gap. Specifically, the nucleation mechanism evolves from a single-pathway type for *n*-nonane/hexanol to a somewhat two-pathway type for *n*-nonane/1-methanol. In contrast, for binary mixtures involving medium-length alcohols, the NFE maps display the most striking feature, with the saddle point stretched almost all the way from the *n*-nonane-enriched to the alcohol-enriched domain, implying that multiple pathways coexist on the nucleation map. These findings have challenged the theory with respect to whether a simplistic view of the nucleation process holds for all systems. In particular, those theoretical models based on the assumption that nucleation proceeds through the formation of mixed critical clusters with a certain well-defined composition would have to be modified accordingly for an accurate prediction of the nucleation rates for these systems.

References and Notes

(1) Zahoransky, R. A.; Peters, F. *J. Chem. Phys.* **1985**, *83*, 6425.
(2) Schmitt, J. L.; Whitten, J.; Adams, G. W.; Zalabsky, R. A. *J. Chem. Phys.* **1990**, *92*, 3693.

(3) Wyslouzil, B. E.; Seinfeld, J. H.; Flagan, R. C.; Okuyama, K. *J. Chem. Phys.* **1991**, *94*, 6827.

(4) Viisanen, Y.; Strey, R.; Laaksonen, A.; Kulmala, M. *J. Chem. Phys.* **1994**, *100*, 6062.

(5) Viisanen, Y.; Wagner, P. E.; Strey, R. *J. Chem. Phys.* **1998**, *108*, 4257.

(6) Wagner, P. E.; Strey, R. *J. Phys. Chem. B* **2001**, *105*, 11656.

(7) Strey, R.; Viisanen, Y. *J. Chem. Phys.* **1993**, *99*, 4693.

(8) Strey, R.; Viisanen, Y.; Wagner, P. E. *J. Chem. Phys.* **1995**, *103*, 4333.

(9) Viisanen, Y.; Strey, R. *J. Chem. Phys.* **1996**, *105*, 8293.

(10) Looijmans, K. N. H.; Luijten, C. C. M.; van Dongen, M. E. H. *J. Chem. Phys.* **1995**, *103*, 1714.

(11) Vohra, V.; Heist, R. H. *J. Chem. Phys.* **1996**, *104*, 382.

(12) Anisimov, M. P.; Koropchak, J. A.; Nasibulin, A. G.; Timoshina, L. V. *J. Chem. Phys.* **1998**, *109*, 10004.

(13) Peters, F.; Rodemann, T. *Exp. Fluids* **1998**, *24*, 300.

(14) Peeters, P.; Hrubý, J.; van Dongen, M. E. H. *J. Phys. Chem. B* **2001**, *105*, 11763.

(15) Heath, C. H.; Streletzky, K. A.; Wyslouzil, B. E.; Wölk, J.; Strey, R. *J. Chem. Phys.* **2003**, *118*, 5465.

(16) Wyslouzil, B. E.; Heath, C. H.; Cheung, J. L.; Wilemski, G. *J. Chem. Phys.* **2000**, *113*, 7317.

(17) Stauffer, D. *J. Aerosol Sci.* **1976**, *7*, 319.

(18) Wilemski, G. *J. Phys. Chem.* **1987**, *91*, 2492.

(19) Jaecker-Voirol, A.; Mirabel, P.; Reiss, H. *J. Chem. Phys.* **1987**, *87*, 4849

(20) Noppel M. *J. Chem. Phys.* **1998**, *109*, 9052.

(21) Zeng, X. C.; Oxtoby, D. W. *J. Chem. Phys.* **1991**, *94*, 4472.

(22) Talanquer, V.; Oxtoby, D. W. *J. Chem. Phys.* **1996**, *104*, 1993.

(23) Napari, I.; Laaksonen, A. *J. Chem. Phys.* **1999**, *111*, 5485.

(24) Oxtoby, D. W. *Acc. Chem. Res.* **1998**, *31*, 91.

(25) ten Wolde, P. R.; Frenkel, D. *J. Chem. Phys.* **1998**, *109*, 9901.

(26) ten Wolde, P. R.; Frenkel, D. *J. Chem. Phys.* **1998**, *109*, 9919.

(27) Oh, K. J.; Zeng, X. C. *J. Chem. Phys.* **2000**, *112*, 294.

(28) Yoo, S.; Oh, K. J.; Zeng, X. C. *J. Chem. Phys.* **2001**, *115*, 8518.

(29) Kusaka, I.; Wang, Z.-G.; Seinfeld, J. H. *J. Chem. Phys.* **1998**, *108*, 3416.

(30) Kusaka, I.; Oxtoby, D. W. *J. Chem. Phys.* **1999**, *110*, 5249.

(31) Chen, B.; Siepmann, J. I.; Oh, K. J.; Klein, M. L. *J. Chem. Phys.* **2001**, *115*, 10903.

(32) Chen, B.; Siepmann, J. I.; Oh, K. J.; Klein, M. L. *J. Chem. Phys.* **2002**, *116*, 4317.

(33) Chen, B.; Siepmann, J. I.; Klein, M. L. *J. Am. Chem. Soc.* **2003**, *125*, 3113.

(34) Chen, B.; Siepmann, J. I.; Klein, M. L. *J. Phys. Chem. A* **2005**, *109*, 1137.

(35) McKenzie, M. E.; Chen, B. *J. Phys. Chem. B* **2006**, *110*, 3511.

(36) Chen, B.; Siepmann, J. I. *J. Phys. Chem. B* **2000**, *104*, 8725.

(37) Chen, B.; Siepmann, J. I. *J. Phys. Chem. B* **2001**, *105*, 11275.

(38) Torrie, G. M.; Valleau, J. P. *Chem. Phys. Lett.* **1974**, *28*, 578.

(39) Wilding, N. B. *Phys. Rev. E* **1995**, *52*, 602.

(40) Potoff, J. J.; Panagiotopoulos, A. Z. *J. Chem. Phys.* **1998**, *109*, 10914.

(41) Siepmann, J. I.; Frenkel, D. *Mol. Phys.* **1992**, *75*, 59.

(42) Frenkel, D.; Mooij, G. C. A. M.; Smit, B. *J. Phys.: Condens. Matter* **1992**, *4*, 3053.

(43) Martin, M. G.; Siepmann, J. I. *J. Phys. Chem. B* **1998**, *102*, 2569.

(44) Wierzchowski, S.; Kofke, D. A. *J. Chem. Phys.* **2001**, *114*, 8752.

(45) Tsangaris, D. M.; de Pablo, J. J. *J. Chem. Phys.* **1994**, *101*, 1477.

(46) Panagiotopoulos, A. Z. *Mol. Phys.* **1987**, *61*, 813.

(47) Panagiotopoulos, A. Z.; Quirke, N.; Stapleton, M.; Tildesley, D. J. *Mol. Phys.* **1988**, *63*, 527.

(48) Smit, B.; de Smedt, P.; Frenkel, D. *Mol. Phys.* **1989**, *68*, 931.

(49) Martin, M. G.; Siepmann, J. I. *J. Phys. Chem. B* **1999**, *103*, 4508.

(50) Chen, B.; Potoff, J. J.; Siepmann, J. I. *J. Phys. Chem. B* **2001**, *105*, 3093.

(51) Martin, M. G.; Siepmann, J. I.; Schure, M. R. *J. Phys. Chem. B* **1999**, *103*, 11191.

(52) Allen, M. P.; Tildesley, D. J. *Computer Simulation of Liquids*; Oxford University Press: Oxford, 1987.

(53) Seok, C.; Oxtoby, D. W. *J. Chem. Phys.* **1998**, *109*, 7982.

(54) Oxtoby, D. W.; Laaksonen, A. *J. Chem. Phys.* **1995**, *102*, 6846.

(55) Talanquer, V.; Oxtoby, D. W. *J. Chem. Phys.* **1997**, *106*, 3673.

(56) Oxtoby, D. W.; Kashchiev, D. *J. Chem. Phys.* **1994**, *100*, 7665.

(57) Ford, I. J. *J. Chem. Phys.* **1996**, *105*, 8324.

(58) Stubbs, J. M.; Siepmann, J. I. *J. Am. Chem. Soc.* **2005**, *127*, 4722.

(59) Stubbs, J. M.; Siepmann, J. I. *J. Phys. Chem. B* **2002**, *106*, 3968.

(60) Chen, B.; Siepmann, J. I. *J. Phys. Chem. B* **2006**, *110*, 3555.